Scanning holographic microscopy of three-dimensional fluorescent specimens

Guy Indebetouw and **Wenwei Zhong**
Department of Physics, Virginia Tech, Blacksburg, Virginia 24061-0435

Abstract

We demonstrate experimentally the three-dimensional reconstructions of fluorescent biological specimens using scanning holographic microscopy. Three-dimensional reconstructions with transverse resolution below about 1 μm of transmission and fluorescence emission images are presented and analyzed. The limitations of the method are discussed.

1. INTRODUCTION

Digital holography was proposed by Goodman and Lawrence[1] as an extension of Gabor's invention[2] and Leith and Upatnieks's first successful demonstration of off-axis holography. [3] With recent advances in high-resolution solid-state array sensors based on charge-coupled device technology (CCD), as well as the availability of ever higher digital computational power and data storage capabilities, digital holography has become an emerging technology with an increasing number of applications in, e.g., metrology, nondestructive testing, and three-dimensional (3D) imaging.[4] In digital holography, the hologram is captured on a 2D array detector as the interference of the wave scattered by the object and a reference wave from the same coherent source. The hologram is then reconstructed digitally by simulating the backpropagation of the light diffracted by the hologram, using Fresnel–Kirchhoff diffraction theory in either real space or spatial frequency space.

A promising application of digital holography is 3D microscopic imaging of biological specimens.[5–7] One attractive advantage of holography in biological imaging is that the entire 3D volume of a thick specimen is acquired in a single 2D scan of the detector. The acquisition speed of 3D information is a major factor in the study of inter- and intracellular dynamical activities. If speed is a major requirement for the study of 3D dynamical processes, so is the use of fluorescent markers for labeling different cellular structural features and tracing their functionalities. Thus, the understanding of dynamical cellular processes requires both high-resolution and short-acquisition-time imaging of 3D fluorescent distributions. Unfortunately, conventional digital holography requires spatial and temporal coherence and is thus not applicable to the capture of holograms of fluorescent specimens.

In the late 1980's, a two-pupil synthesis method was proposed by Lohmann and Rhodes as a means of achieving incoherent optical imaging and processing with bipolar (and, in general, complex) point-spread functions.[8] To construct a Gabor hologram, each object scatterer must be encoded as a complex spherical wave. This could be achieved with incoherent objects, using the two-pupil synthesis method, as was recognized by Poon and Korpel.[9] The original idea, which was later called scanning holography,[10] is to scan the object in a 2D raster with the desired complex point-spread function created by the interference of the two diffraction distributions emerging from each pupil. A temporal frequency offset is introduced between the two pupils, and the desired signal from a spatially integrating detector is obtained using a heterodyne method. With today's high-speed data acquisition systems with deep memory, other ways of capturing and demodulating the data are possible. The applications of scanning

holography to high-resolution microscopy has been studied theoretically,[11] and preliminary results showing the reconstruction of holograms of large fluorescent beads have been published.[12] More recent analyses[13,14] supported by experimental verifications[15] have revealed that scanning holographic microscopy based on two-pupil synthesis opens up a wide range of possibilities for synthesizing unusual point-spread functions. Examples include pupils leading to transverse resolution limits exceeding the Rayleigh limit of the objective, to imaging with extended depth of focus (DOF) with elimination of the out-of-focus flare that obscures the wide-field images of thick specimens, or to edge enhancement and optical sectioning using pupils with an overlap interaction region confined to a thin axial section of the specimen.[14]

Compared with established methods of fluorescence microscopy,[16] the holographic method has three potential advantages. Two of them, namely, the potential for high acquisition rates and the flexibility in point-spread function design, have already been mentioned. In addition, the phase information of the reconstructed image amplitude can be exploited for quantitative microtopology and to achieve *a posteriori* axial sectioning. These topics are presently being studied and will not be treated in this paper. The holographic method has also its limitations. An important one is that, without additional processing, the reconstructed images are comparable with wide-field images. Indeed, the holographic method is not conducive to optical sectioning, since its main advantage is to acquire the entire volume information simultaneously. The deconvolution and restoration methods commonly used in wide-field microscopy can also be used to improve the holographic reconstructions. How the application of these methods compares with the sectioning capability of, e.g., confocal microscopy[16] appears to depend critically on the nature of the specimen and its environmental conditions.[17,18]

The goal of this paper is to illustrate experimentally how scanning holographic microscopy is used to capture holograms of fluorescent biological samples and reconstruct 3D images. The spatial resolution of the system described is of the order of 1 μm. We also show that the method is conducive to the simultaneous acquisition of several holograms in different imaging modes such as, for example, transmission, reflection, and fluorescence excitation and emission at different wavelengths, which may be an important asset in biodynamics studies. The paper is organized as follows. For completeness, the theoretical background is briefly reviewed in Section 2. The details of the experimental system are given in Section 3. We also show in Section 3 examples of 3D reconstructions of thick biological specimens. In Section 4, we demonstrate that it is possible to compensate for the phase aberrations of the optics by reconstructing the hologram using a correlation with the experimental hologram of a subresolution point object rather than using the usual Fresnel–Kirchhoff propagation integral. Holographic reconstructions of 3D fluorescent specimens with resolution of the order of 1 μm are presented, apparently for the first time, in Section 5. These images are discussed, and details of some unusual observations in the reconstruction of holograms of thick fluorescent specimens are explained.

2. THEORETICAL BACKGROUND

Figure 1 is a sketch of a generic two-pupil synthesis imaging system in scanning mode. In general, arbitrary complex amplitude distributions of the two pupils can be realized using spatial light modulators. For the implementation of scanning holographic microscopy, as discussed here, one of the two pupil distributions consists of a point source (focused beam), and the other consists of a spherical wave filling the entrance pupil of the objective. These distributions are easily realized with spherical lenses, as shown in Fig. 2. The diffraction distributions from the two pupils are displayed in the focal plane of the objective, where they interfere. The specimen is placed in that plane, on a 2D scanning stage. The two pupil distributions needed to record the in-line single-sideband hologram of an incoherent or fluorescent specimen are[11]

$$\mathcal{P}_1(u, v) \sim \delta(u, v),$$

$$\mathcal{P}_2(u, v) = \exp\left\{-ikz_0[1 - \sqrt{1 - \lambda^2(u^2 + v^2)}]\right\}\mathcal{P}_0(u, v). \tag{1}$$

In these expressions, (u,v) are the transverse spatial frequency coordinates in the pupil plane. The tilde indicates the Fourier (spatial frequency) domain. $\delta(u,v)$ is a Dirac delta function approximating a beam focused at the center of the pupil to a subresolution size. $k=2\pi/\lambda$ is the wave number of the excitation radiation, and λ is its wavelength.

$\mathcal{P}_0(u, v) = 1$ if $\sqrt{u^2 + v^2} < \rho_{MAX} = \sin(a)/\lambda$, and $=0$ otherwise, is the support of the pupil. $\sin(\alpha)=NA$ is the numerical aperture of the objective. The pupil distributions of expressions (1) are chosen to produce, in object space, two diffraction distributions consisting of a plane wave from the pupil $\mathcal{P}_1(u, v)$ and, in the paraxial approximation, a spherical wave of the form

$$P_2(x, y) \sim (i\lambda z_0)^{-1} \exp[i\pi(x^2 + y^2)/\lambda z_0]\text{circ}[\sqrt{x^2 + y^2}/z_0 \sin(a)],$$

from the pupil $\mathcal{P}_2(u, v)$. The parameter z_0 represents the radius of curvature of that spherical wave in the focal plane of the objective (Fig. 1). This is a free parameter in the design of the system, and it can be used to adapt the size of the scanning distribution to a particular specimen without changing the NA. The temporal frequency of one of the pupils is shifted by a known amount Ω [using, e.g., an electro-optic phase modulator (EOM) or an acousto-optic device], in order to be able to demodulate the detected signal in the temporal domain and extract the interference term representing the pupil interaction. The demodulation can be achieved by, e.g., heterodyne detection or bandpass filtering in Fourier space.

The 3D interference distribution projected through the objective on the specimen is $|P_1(x,y,z) + P_2(x,y,z)\exp(i\Omega t)|^2$, and the interference term, hereafter called the scanning distribution, is

$$S(x, y, z) = P_1^*(x, y, z)P_2(x, y, z). \tag{2}$$

The asterisk indicates a complex conjugate, and z is the axial coordinate in object space measured from the focal plane of the objective. $P_j(x,y,z)$, $j=1,2$, are the 3D inverse Fourier transforms of the generalized pupils defined by McCutchen.[19] Namely,

$$P_j(x, y, z) = \int du\, dv\, dw\, \mathcal{P}_j(u, v) \exp\left\{i2\pi(ux + uy + wz)\right\}\delta(\lambda^{-1} - \sqrt{u^2 + v^2 + w^2}). \tag{3}$$

In this expression, (u,v,w) are the 3D spatial frequency coordinates for a monochromatic radiation with wavelength λ. Using Eqs. (1)–(3), we find the scanning distribution to be

$$S(x, y, z) = \int du\, dv\, \exp[i2\pi(ux + uy)] \exp\left\{-ik(z_0 + z) \times [1 - \sqrt{1 - \lambda^2(u^2 + v^2)}]\right\}\mathcal{P}_0(u, v). \tag{4}$$

The 2D transverse scan of the specimen effects a spatial convolution of the 3D object intensity distribution $I(x,y,z)$ with the 3D scanning distribution. A spatially integrating detector captures a temporal signal, which, after demodulation and reformatting, gives the 2D single-sideband hologram

$$H(x, \ y) = \int dz I(x, \ y, \ z) \otimes S(x, \ y, \ z), \tag{5}$$

where $\otimes$ symbolizes a 2D convolution integral over the transverse coordinates. One important advantage of the scanning method is the mapping of the space domain to the time domain. As a result of this mapping, the bandpass filtering operation necessary to demodulate the signal can be performed digitally in the time domain. Since no spatial coherence is required, the method is applicable to fluorescent specimens. Furthermore, the method allows the direct capture of a single-sideband hologram, without zero order and without twin image.

The reconstruction of the hologram focused at a chosen depth z_R (measured from the focal plane of the objective) is effected by a correlation with the cross section of the scanning distribution at the desired axial position, $z = z_R$. Thus, the reconstruction can be written as

$$R(x, \ y, \ z_R) = H(x, \ y) \oplus S(x, \ y, \ z_R) = H(x, \ y) \otimes S^*(x, \ y, \ z_R), \tag{6}$$

where $\oplus$ symbolizes a 2D correlation and the last equality holds if $S(x,y,z)$ has circular symmetry. The reconstruction expressed in Eq. (6) can be realized in two ways. In the paraxial approximation, the correlation with a spherical wave with curvature radius $(z_0 + z_R)$ is equivalent to a Fresnel–Kirchhoff backpropagation for that distance. This is the usual way digital holograms are reconstructed. It is also possible to use the experimental distribution from the hologram of a subresolution point object. As will be shown in Section 3, this allows for the compensation of the phase aberrations of the system.

In Fourier space, Eq. (6) reads as

$$\mathcal{R}(u, \ v; z_R) = \int dz \mathcal{I}(u, \ v; z) \mathcal{S}(u, \ v; z) \mathcal{S}^*(u, \ v; z_R). \tag{7}$$

The absolute value of the complex reconstruction is thus proportional to the object intensity (transmittance or reflectance) or to the concentration of fluorescent dye, in the case of a fluorescent specimen. The overall imaging transfer function, which expresses the transfer of a spatial frequency with transverse components (u,v) from the axial plane z in object space to the axial plane z_R of the reconstruction, is defined as

$$\begin{aligned} \mathcal{T}(u, \ v; z - z_R) &= \mathcal{S}(u, \ v; z) \mathcal{S}^*(u, \ v; z_R) \\ &= \exp\left\{ -ik(z - z_R)[1 - \sqrt{1 - \lambda^2(u^2 + v^2)}] \right\} \\ &\times \left| \mathcal{P}_0(u, \ v) \right|^2. \end{aligned} \tag{8}$$

Since $w = \sqrt{\lambda^{-2} - (u^2 + v^2)}$ is the longitudinal component of the 3D spatial frequency vector, the transfer function of Eq. (8) is identical to the coherent transfer function of an imaging system with a pupil $\left| \mathcal{P}_0(u, \ v) \right|^2$ from which the phase representing the uniform axial travel $(z - z_R)$ has been subtracted. In particular, the modulation transfer function $| \mathcal{T}(u, \ v) |^2$ is unity for all the spatial frequencies transmitted, up to the cutoff ρ_{MAX} of the objective. The infocus plane $z = z_R$ is reconstructed with the ideal in-focus transfer function $\left| \mathcal{P}_0(u, \ v) \right|^2 = 1$ within the domain of the pupil, and the out-of-focus information is $(z \neq z_R)$ is reconstructed with a phase proportional to the defocus distance $z - z_R$.

3. EXPERIMENTAL SYSTEM AND THREE-DIMENSIONAL RECONSTRUCTION

The following results were obtained with the setup sketched in Fig. 2 with the following settings. The scanning distribution was obtained by the interference of a quasi-plane wave from a subresolution pointlike pupil and a spherical wave from a pupil with spherical curvature [expressions (1)]. Both pupils are illuminated with light from a diode-pumped solid-state laser (Verdi from Coherent with $\lambda=532$ nm). Typical laser powers used in these experiments are <10 mW. The objective is a Mitutoyo 20× Plan Apo with a focal length of 10 mm and a nominal NA of 0.42. The radius of curvature of the spherical wave in the focal plane of the objective ($z=0$) is chosen to be $z_0 \sim 150$ μm. The scanning distribution in the plane $z=0$ has a Fresnel number $N_F \approx 15$ and a diameter $2a \approx 70$ μm. Its effective NA is thus $NA=\sin \alpha = \lambda N_F/a \sim 0.23$. This is the NA of the scanning distribution that determines the theoretical resolution limit of the reconstructed images. With this setup, the resolution limits are $\Delta x \sim \lambda/2 \sin \alpha \sim 1$ μm transversally and $\Delta z \sim \lambda/4 \sin^2(\alpha/2) \sim 10$ μm axially. In this experiment, the effective NA of the scanning distribution is lower than that of the objective because the size of the scanning pattern was stopped down by an aperture in order to reduce the amount of stray light. There is, however, no theoretical reason preventing the realization of a scanning pattern having the same NA as that of the objective. In this case, we expect the reconstructed images to be comparable with wide-field images obtained with the same objective. Figure 3(a) shows the phase modulo 2π of the scanning distribution in the plane $z=0$. This distribution was obtained as the hologram of a 1 μm pinhole. The size of this point object is of the same order as the expected resolution but not much smaller. Consequently, the intensity distribution of the hologram is expected to differ from the intensity distribution of the scanning distribution. The phase distribution shown in Fig. 3(a) is, however, a correct representation of the phase of the scanning distribution. The reconstruction of the 1 μm pinhole using Fresnel–Kirchhoff backpropagation is shown in Fig. 3(b). This reconstruction of a quasi-subresolution point object gives a good measure of the point-spread function of the system. Figure 3(c), which will be discussed in the Section 4, is the reconstruction with aberration compensation.

The temporal phase of one of the pupils is offset by 12.5 kHz using a saw tooth-driven EOM (Linos LM0202). The sampling rate of the data acquisition system (Gage Scope CS1602) was 50 k sample/s. The specimen is mounted on a piezoscanning stage (PI Hera 625) driven at a rate of 0.3 s per 200 μm line (including accelerations and return times). With the present system, the data acquisition time is of several minutes per hologram. This rather slow rate is limited by the mechanical scanner and the EOM drive. It is useful to project what could be expected from the holographic method using up-to-date high-speed mirror scanning technology and acousto-optic modulators. In this case, the acquisition rate is limited by the signal-to-noise ratio (SNR). Assuming that shot noise (or photon noise) is the limiting factor, the SNR is equal to the average photon flux divided by twice the bandwidth of the detection system.[20] The Nyquist criterion demands that the bandwidth be at least twice the sampling rate f_S, which should itself be at least twice the modulation frequency f_M. If the desired dimension of the hologram matrix is $N \times N$ pixels after demodulation, the raw data consist of N lines with $M>2N$ samples per line. The shortest time needed to acquire the hologram is $T>2N^2/f_S$, and the detection bandwidth must be at least $B>4N^2/T$. Consequently, the minimum photon flux required to acquire a $N \times N$ hologram in a time T with a SNR is $\Phi>8(SNR)/T$. For example, the acquisition of a 2000×2000 hologram matrix in 1 s with a SNR=100 (20 dB) requires a minimum average photon flux of 3.2×10^9 photon/s. If the source is unable to produce the required flux because of possible bleaching or other photo-damage, there are two alternatives. Either the acquisition time must be increased or the hologram matrix must be reduced in size, at the price of possibly reducing the system's resolution.

In our system, the raw data are read on-line to the computer memory while the scanning takes place. The collected data are then treated using MatLab codes to construct the hologram using the following procedure. Each line is cut from the temporal data stream, eliminating the periods of acceleration and return of the scanner. The initial phase of the modulation of each line is realigned using a reference signal collected simultaneously with the data (see Fig. 2). This step cancels out all possible phase errors due to a lack of synchronization among the scanner, the modulation, and the data acquisition clock, as well as those due to possible phase drifts of the carrier due to electronic or mechanical fluctuations. The modulated lines with 10^4 samples each are then bandpass filtered around the modulation frequency. Finally, the lines are stacked to form a 2D single-sideband in-line hologram of the sample with 2000×2000 samples. This number of pixels was found to be adequate to represent the phase of the hologram accurately. With a Pentium dual processor D-820+, 2.80 GHz, 3.0 GB RAM, it takes less than 15 s to cut the data string, filter the signal, and construct the 2D single-sideband hologram. Once the hologram is stored, it takes less than 60 s to reconstruct a stack of ten axial images.

Figure 4 shows the reconstructed intensity of several *Oscillatoria* strands (small algae slide from Carolina Biological Supply). The absolute value of the complex single-sideband hologram from which these images are reconstructed is shown in Fig. 5. The hologram was obtained by spatially integrating the light of the scanning distribution transmitted and scattered by the sample at 532 nm. The reconstructions are obtained by Fresnel backpropagation to three reconstruction planes in which different strands are in focus. The focal positions of the reconstructed planes are 130, 155, and 180 μm from the center of curvature of the spherical wave of the scanning distribution. In Fig. 4(a), with $z=-20$ μm from the focal plane of the objective, the SW-to-NE strand is in focus. In Fig. 4(b), with $z= +5$ μm from the focal plane of the objective, the NW-to-S strand is in focus. In Fig. 4(c), with $z= +30$ μm from the focal plane of the objective, the NW-to-SE strand is in focus.

4. ABERRATION COMPENSATION

The reconstruction of the holograms using digital Fresnel–Kirchhoff propagation may not lead to the best result. One of the reasons for this is that with high-NA objectives, the scanning distribution that is projected through the objective is the interference of two waves that do not match the objective's design. Even if one of the waves can be adapted to the best correction of the objective, the other will not. Consequently, the scanning distribution will contain unavoidable phase aberrations. With perfect alignment, spherical aberration is the most severe. There are other sources of aberrations that are difficult to avoid. For example, the nonplanar waves transmitted through cube beam splitters and dichroic filters acquire additional spherical aberrations as well as astigmatism if the filters are tilted at some angles, as is often necessary. The severity of these aberrations (spherical and astigmatism) is clearly apparent in the reconstruction of the pinhole shown in Fig. 3(b). Some of these aberrations can be corrected if the hologram is reconstructed by using a correlation with the experimental scanning distribution rather than using the theoretical Fresnel diffraction integral. If the actual experimental scanning distribution is used for reconstruction, the wavefront aberrations present in the hologram are canceled out by the correlation with the reconstruction function recorded experimentally with the same aberrations, as Eq. (7) indicates. In practice, the scanning distribution can be obtained experimentally as the hologram of a subresolution point object placed in the objective's focal plane ($z=0$). To reconstruct the hologram in a different plane ($z=z_R$), this distribution is then propagated digitally to the desired reconstruction plane. The reconstruction of the 1 μm pinhole using this method is shown in Fig. 3(c). The compensation of the aberrations present in Fig. 3(b), which was reconstructed using digital Fresnel–Kirchhoff propagation, is evident.

To implement this idea with the *Oscillatoria* specimen, the hologram of the 1 μm pinhole was recorded using the same settings as for the hologram of the specimen. As mentioned, the phase of this hologram is a good representation of the phase of the scanning distribution, including its eventual aberrations. This phase distribution, with amplitude equalized to unity, is propagated digitally to the desired reconstruction plane and used in Eq. (6) to reconstruct the section of the 3D specimen corresponding to that particular plane. The reconstructions of the *Oscillatoria* strands using the experimental scanning distributions are shown in Figs. 6(a)–6(c).

One should note that the experimental scanning distribution used to reconstruct the hologram with aberration compensation need not be recorded each time new data are taken. For given distributions of the two pupils, and a given objective, the scanning distribution is fixed and is independent of the exact axial position of the objective. This means that the experimental scanning distribution used for reconstruction remains valid even if the objective has to be refocused to accommodate different specimens. In some of our experiments, data were reconstructed, without apparent losses, with a scanning distribution captured several days earlier with the same setup and the same objective.

5. FLUORESCENCE HOLOGRAMS

In this section we present, apparently for the first time, high-resolution reconstructions of 3D fluorescent specimens recorded holographically. Two of the *Oscillatoria* strands of the previous sample had been stained with phloxine, a dye that fluoresces when excited at 532 nm. The other strands were stained with a nonfluorescent blue dye. Holograms were recorded using the same scanning distribution at 532 nm as was used for the previous results but with the detector collecting the fluorescence emission. For comparison, the fluorescent emission was collected in both reflection and transmission and detected by two spatially integrating detectors through notch filters at 600 nm. The amplitude (proportional to the dye concentration) of two sections reconstructed from the hologram of the fluorescent *Oscillatoria* recorded in reflection are shown in Fig. 7. The two sections have axial positions 130 and 180 μm. The strand located at 155 μm, which is visible in Figs. 4 and 6, does not fluoresce and is thus not visible in this imaging mode.

The appearance of a conspicuous speckle in these images is unexpected because we are dealing with fluorescence emission that is spatially incoherent. Of course, the excitation field is a spatially coherent scanning distribution, but that same distribution does not produce speckle in the reconstruction of the transmission images shown in Figs. 4 and 6. We speculate that this specklelike effect is due to the presence of random inhomogeneities in the distribution of fluorescent dye throughout the volume of the specimen. Several tests were carried out to check this hypothesis. A first clue is given by the representation of the phase of the reconstructions shown in Fig. 8. The speckle is clearly related to that phase distribution. We also recorded the hologram of the same specimen but collected the fluorescence emission in transmission rather than in reflection. The amplitude and phase of the reconstruction of this hologram, at the same axial positions as before, are shown in Figs. 9 and 10. The reconstructions of the transmission hologram are almost identical to the reconstructions of the reflection hologram (Figs. 7 and 8) but with notable differences. The transmission images show two features indicated by arrows in Fig. 10, which are obviously due to the presence of the two nonfluorescent strands seen in Figs. 4 and 6. These features are particularly noticeable in the phase images. In the images obtained in reflection, only one of the features is present, as indicated by the arrow in Fig. 8. This observation indicates that the SW-to-NE fluorescent strand is closest to the objective, since its reflection is not affected by the presence of other features below, while its transmission is affected. The NW-to-SE fluorescent strand, however, must be furthest from the objective, since both its reflection and its transmission images are affected by the nonfluorescent leaves

above it. This geometry is, of course, confirmed by the 3D reconstruction in Fig. 4, but this observation indicates that the phase of the reconstruction, which is not directly related to the phase of the specimen but rather to the axial positions of the imaged features, could, if properly quantified, be exploited for metrological purposes.

The specklelike phenomenon just described appears to be due to 3D inhomogeneities in the fluorescent dye distribution. From Eqs. (7) and (8), it is apparent that the complex amplitude of the reconstruction of a point object $\delta(0,0,z)$ with axial position z, reconstructed in plane z_R is, at the transverse location of that point, $R(0, 0, z - z_R) = \int \tilde{T}(u, v; z - z_R) \mathrm{d}u\mathrm{d}v$. In cylindrical coordinates, the complex amplitude at the location of the reconstructed point is found to be

$$R(0, z - z_R) = \pi(\rho_{\mathrm{MAX}})^2 \exp(i\varDelta) \sin(\varDelta) \big/ \varDelta,$$
$$\varDelta = (\pi \big/ 2)\lambda(z - z_R)(\rho_{\mathrm{MAX}})^2.$$

(9)

This expression shows that the point reconstruction exhibits a phase proportional to the defocus distance and that this phase varies by $\pi/2$ for a defocus distance equal to one depth of focus ($DOF = \lambda/\sin^2(\alpha) = 1/\lambda(\rho_{\mathrm{MAX}})^2$). The other factor in Eqs. (9) represents the amplitude drop due to defocusing. This result was confirmed experimentally by recording a hologram of a 3D distribution of fluorescent beads (diameter 6 μm). The reconstruction in a particular plane of focus shows that, at the location of a particular bead, the phase is proportional to the axial position of that bead. No speckle appears in these reconstructions because the sample consists of uniformly fluorescent objects. These observations indicate that, if the specimen contains a random distribution of residual fluorescent centers within the volume of the mounting medium, the reconstruction of this 3D random distribution will exhibit a speckle appearance resembling that observed in coherent imaging. The origin of the speckle is quite different in the two cases, however. In coherent imaging, the speckle is due to the coherent superposition of the images of random scatterers with random phase. Here the phase scales as 2π per wavelength. In the reconstruction of thick fluorescent specimens recorded holographically, the speckle is due to the superposition of random fluorescent centers reconstructed with a phase scaling as $\pi/2$ per DOF. In Figs. 8 and 10, the residual fluorescence responsible for the speckle appears in the mounting medium along the sides of the *Oscillatoria* strands. If this interpretation of the speckle effect is correct, high-contrast speckle is expected to appear only if the range of the random phase spans at least 2π. From Eqs. (9), this is the case if the specimen thickness is at least four times the DOF. The *Oscillatoria* sample satisfies this condition (thickness ~60 μm, DOF~10 μm). To test this hypothesis further, the hologram of fluorescent pollen grains, also dyed with phloxine and excited at 532 nm, was recorded using the same scanning distribution as for the *Oscillatoria*. The hologram was recorded by collecting the spatially integrated reflected emission at 600 nm. The amplitude and the phase of the reconstruction are shown in Fig. 11. This sample is thinner (~20 μm or less) and more homogeneous than the *Oscillatoria*. As expected, the reconstruction exhibits a much less conspicuous speckle effect.

6. SUMMARY

We have demonstrated, apparently for the first time, the recording and 3D reconstruction of holograms of fluorescent biological specimens with micrometer-sized spatial resolution. Scanning holographic microscopy making use of the two-pupil synthesis method was used to record inline single-sideband holograms of incoherent absorbing and fluorescent specimens of algae and pollen grains. The limitations of the method are discussed. It is shown that the reconstructed images contain phase information that is related not to the phase of the specimen but to its axial position relative to the plane of reconstruction. With thick inhomogeneous

random fluorescent dye distributions, this phase leads to a specklelike effect. Homogeneous and thin specimens do not exhibit this phenomenon. This phase information could be exploited to obtain quantitative topological measures of reflective specimens (integrated circuit chips, microelectromechanical systems, etc.). It could also be exploited to extract sectioned images from the holographic reconstructions. These topics are presently under study.

References

1. Goodman JW, Lawrence RW. "Digital image information from electronically detected holograms,". Appl Phys Lett 1967;11:77–79.

2. Gabor D. "A new microscopic principle,". Nature 1948;161:777–778.

3. Leith EN, Upatnieks J. "Reconstructed wavefronts and communication theory,". J Opt Soc Am 1962;52:1123–1130.

4. Schnars U, Juptner WPO. "Digital recording and numerical reconstruction of holograms,". Meas Sci Technol 2002;13:R85–R101.

5. E. Cuche, P. Poscio, and C. Depeursinge, "Optical tomography at the microscopic scale by means of a numerical low-coherence holographic technique," in Optical and Imaging Techniques for Biomonitoring II, H. J. Foth, R. Marchesini, and H. Podbielska, eds., Proc. SPIE 2927, 61–66 (1996).

6. Xu W, Jerico MH, Meinertzhagen IA, Kreuzer HJ. "Digital in-line holography for biological applications,". Proc Natl Acad Sci USA 2002;98:11301–11305. [PubMed: 11572982]

7. Cuche E, Bevilacqua F, Depeursinge C. "Digital holography for quantitative phase-contrast imaging,". Opt Lett 1999;24:291–293. [PubMed: 18071483]

8. Lohmann AW, Rhodes WT. "Two-pupil synthesis of optical transfer functions,". Appl Opt 1978;17:1141–1151.

9. Poon TC, Korpel A. "Optical transfer function of an acousto-optic heterodyning image processor,". Opt Lett 1979;4:317–319.

10. Poon TC. "Scanning holography and two-dimensional image processing by acousto-optic two-pupil synthesis,". J Opt Soc Am A 1985;2:521–527.

11. Indebetouw G, Klysubun P, Kim T, Poon TC. "Imaging properties of scanning holographic microscopy,". J Opt Soc Am A 2000;17:380–390.

12. Schilling B, Poon TC, Indebetouw G, Storie B, Shinoda K, Wu M. "Three-dimensional holographic fluorescence microscopy,". Opt Lett 1997;22:1506–1508. [PubMed: 18188283]

13. Indebetouw G. "Properties of a scanning holographic microscope: improved resolution, extended depth of focus, and/or optical sectioning,". J Mod Opt 2002;49:1479–1500.

14. Indebetouw G, Zhong W, Chamberlin-Long D. "Point-spread function synthesis in scanning holographic microscopy,". J Opt Soc Am A 2006;23:xxx–xxx .

15. Indebetouw G, El Maghnouji A, Foster R. "Scanning holographic microscopy with transverse resolution exceeding the Rayleigh limit and extended depth of focus,". J Opt Soc Am A 2005;22:829–898.

16. A. Diaspro, ed., Confocal and Two-Photon Microscopy: Foundation, Applications, and Advances (Wiley, 2002).

17. P. Shaw, "Comparison of wide-field deconvolution and confocal microscopy for 3D imaging," in Handbook of Biological Confocal Microscopy, 2nd ed., J. B. Pawley, ed. (Plenum, 1995), pp. 373–387.

18. Verveer PJ, Gemkow MJ, Jovin TM. "A comparison of image restoration approaches applied to three-dimensional confocal and wide-field fluorescence microscopy,". J Microsc 1999;183:50–61. [PubMed: 12558687]

19. McCutchen CW. "Generalized aperture and the three-dimensional diffraction image,". J Opt Soc Am 1964;54:240–244.

20. B. E. A. Saleh and M. C. Teich, Fundamentals of Photonics (Wiley, 1991).
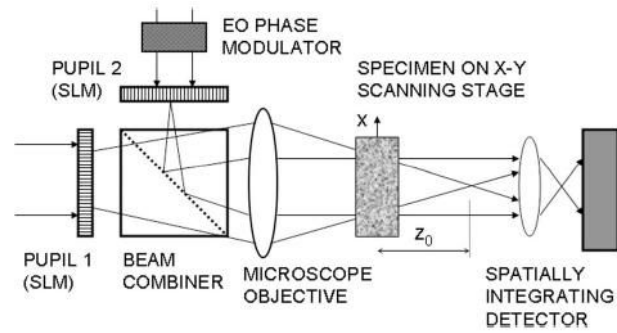
Fig. 1.
Generic sketch of a two-pupil synthesis set up in scanning mode. SLM, spatial light modulator; EO, electro-optic.
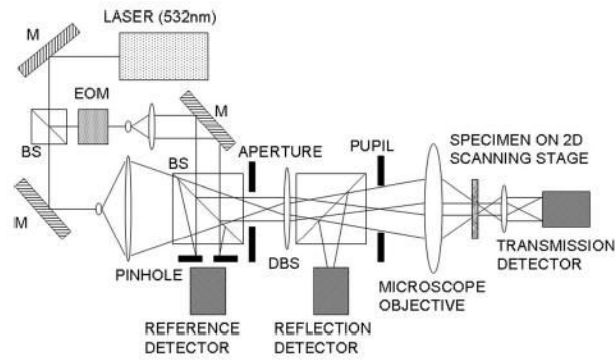
Fig. 2.
Sketch of a scanning holographic microscope based on two-pupil synthesis. M, mirror; BS, beam splitter; DBS, dichroic beam splitter; EOM, electro-optic phase modulator; microscope objective, Mitutoyo Plan Apo 20×, NA 0.42.
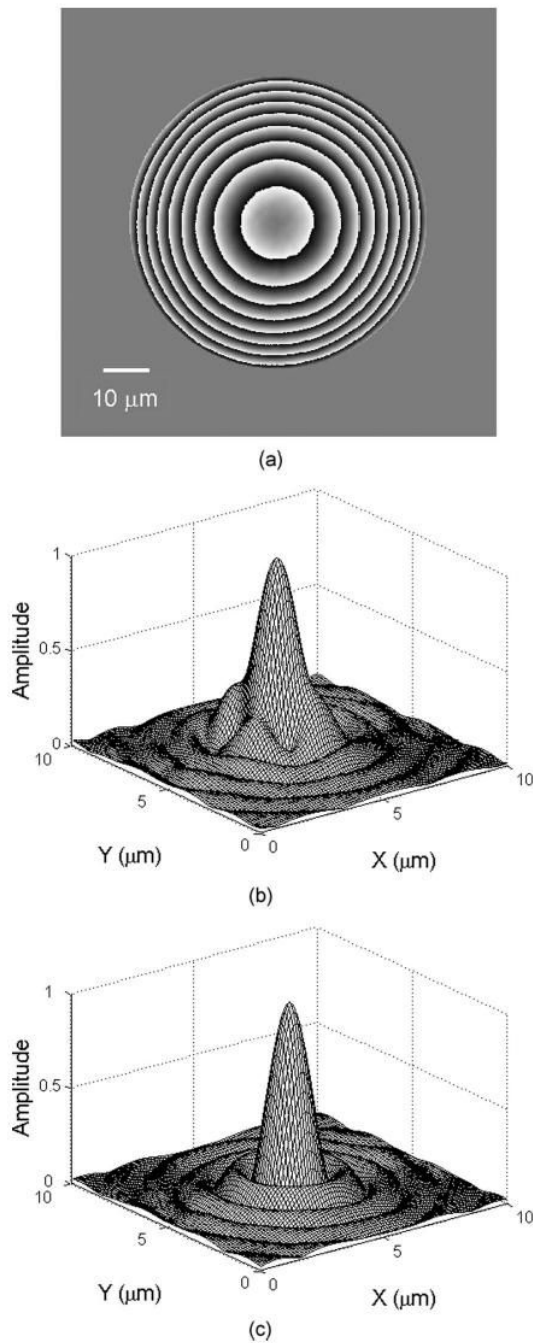
Fig. 3.
(a) Phase distribution modulo 2π of the scanning distribution obtained from the hologram of a 1 μm pinhole. Diameter ~70 μm. Fresnel number ~15. Effective NA ~0.23. (b) Amplitude of the reconstruction of the pinhole using Fresnel–Kirchhoff propagation, representing the in-focus point-spread function with obvious spherical aberration and astigmatism. (c) Amplitude of the reconstruction of the pinhole by correlation with the experimental scanning distribution, showing aberration compensation.
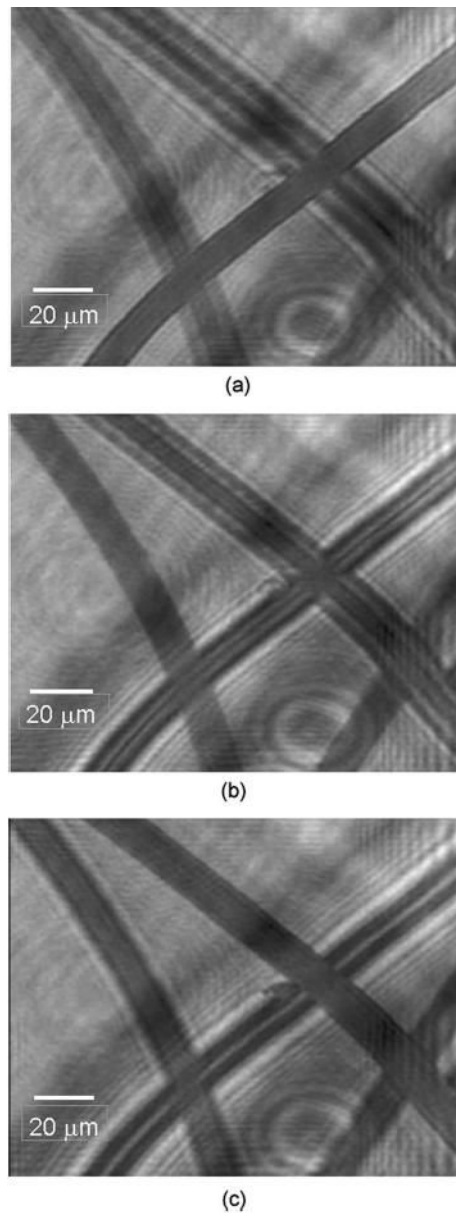
Fig. 4.
Reconstruction of the intensity transmission of *Oscillatoria* leaves (small algae) at three axial positions from the center of curvature of the scanning distribution: (a) z=130 μm, (b) z =155 μm, (c) z=180 μm. The reconstructions were obtained using digital Fresnel–Kirchhoff backpropagation to the desired axial planes.
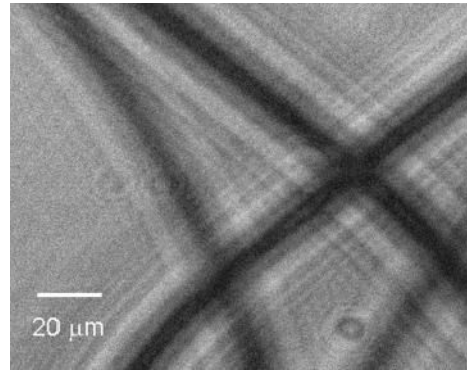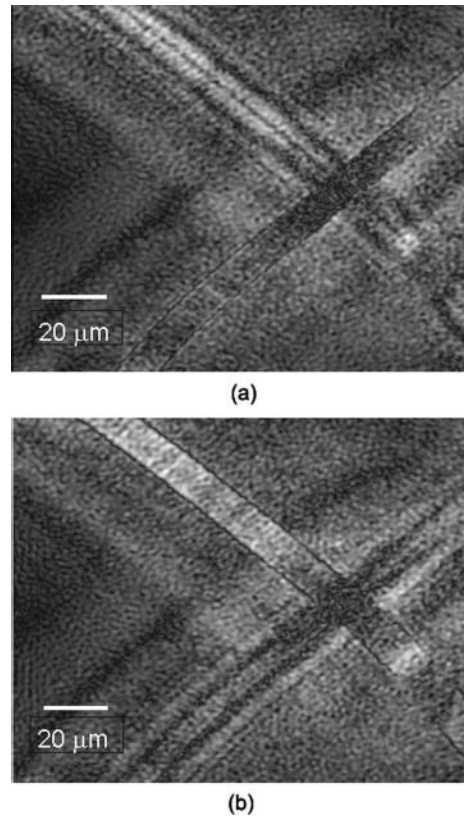
Fig. 5.
Absolute value of the complex single-sideband hologram from which the images of Fig. 4 are reconstructed.
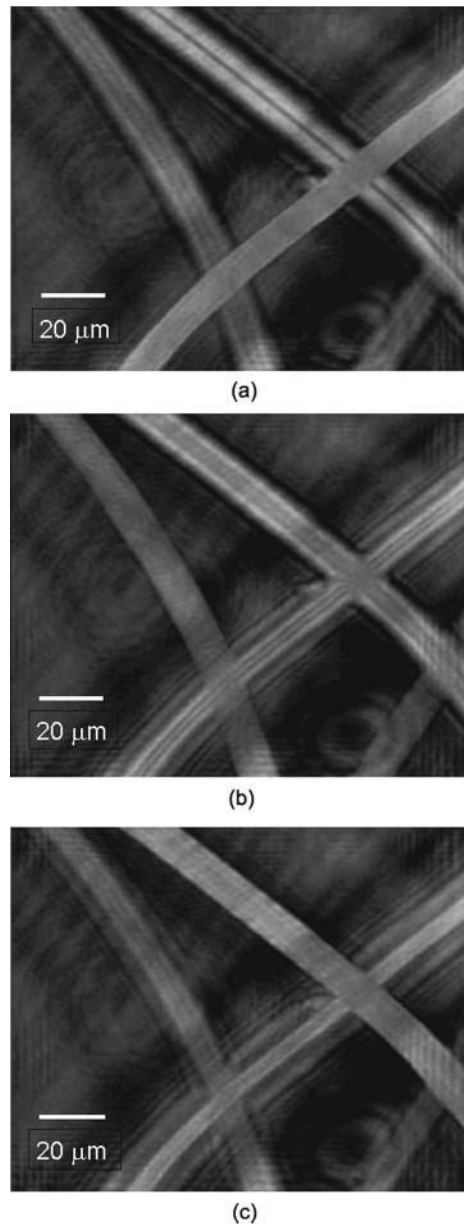
Fig. 6.
Intensity of the reconstruction of the same hologram shown in Fig. 5 but reconstructed by correlation with the phase of the experimental scanning distribution and equalized amplitude.
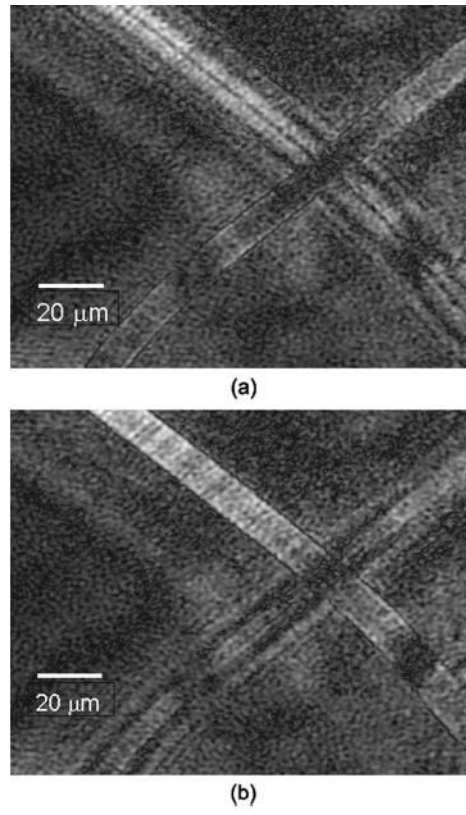
Fig. 7.
Amplitude of the reconstructions of the hologram of fluorescent *Oscillatoria* dyed with phloxine. The amplitude is proportional to the dye concentration. Excitation: 532 nm. Fluorescence emission: 600 nm. Hologram recorded with fluorescence reflection. (a) *z*=130 μm, (b) *z*=180 μm.
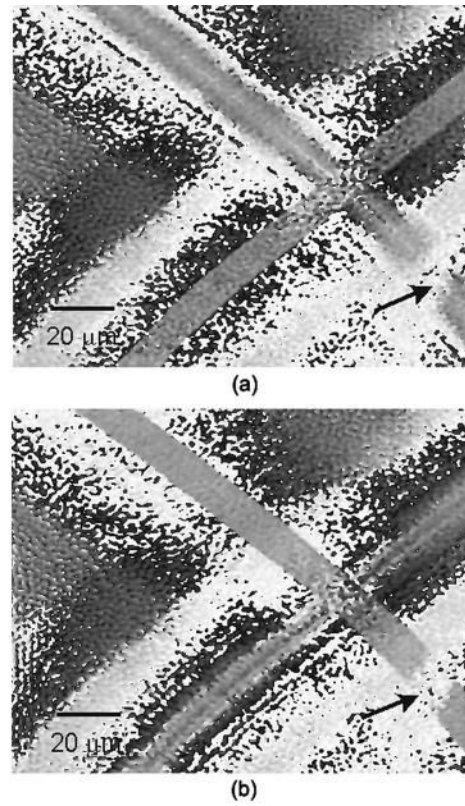
Fig. 8.
Phase (modulo 2π) of the reconstruction of the two sections shown in Fig. 7. The arrows point to two disturbances due to the nonfluorescent strands located between the two fluorescent ones.

Fig. 9.
Same as Fig. 7 but for a hologram recorded with fluorescence transmission.
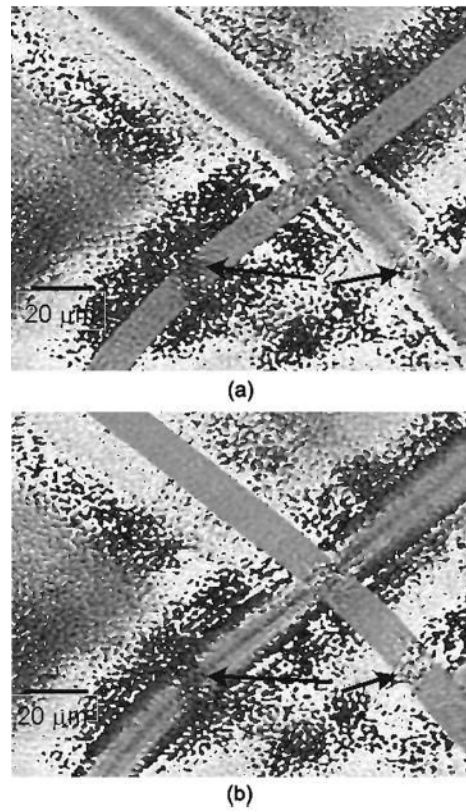
Fig. 10.
Phase (modulo 2π) of the reconstructions of the two sections shown in Fig. 9. The arrows point to two disturbances due to the nonfluorescent strands located between the two fluorescent ones.
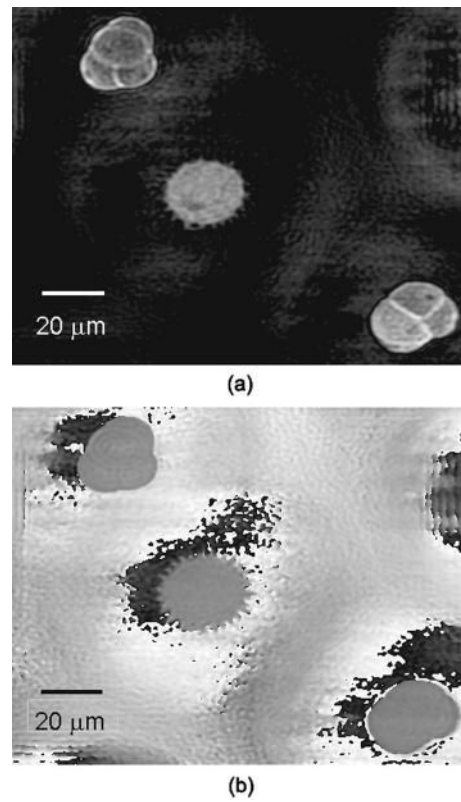
Fig. 11.
(a) Amplitude and (b) phase of the reconstruction of a hologram of fluorescent pollen grains stained with phloxine. Excitation: 532 nm. Emission: 600 nm. Hologram recorded with fluorescence reflection and reconstructed using the experimental scanning distribution for aberration compensation.